Oxygenated deep waters fed early Atlantic overturning circulation upon Antarctic glaciation

Huanye Wang[1], Weiguo Liu[1], Hongxuan Lu[1], Yancheng Zhang[2,3], Yu Liang[2,4], Yuxin He[5], Steven M. Bohaty[6], Paul A. Wilson[6*], Zhonghui Liu[1,2,7*]

[1] State Key Laboratory of Loess and Quaternary Geology, Institute of Earth Environment, Center for Excellence in Quaternary Science and Global Change, Chinese Academy of Sciences, Xi'an 710061, China

[2] Department of Earth Sciences, The University of Hong Kong, Hong Kong, China

[3] School of Marine Sciences, Sun Yat-sen University, Zhuhai 519082, China

[4] School of Earth Resources, China University of Geosciences, Wuhan 430079, China

[5] Key Laboratory of Geoscience Big Data and Deep Resource of Zhejiang Province, School of Earth Sciences, Zhejiang University, Hangzhou 310027, China

[6] University of Southampton, Waterfront Campus, National Oceanography Centre Southampton, SO14 3ZH, UK

[7] Institute of Climate and Carbon Neutrality, The University of Hong Kong, Hong Kong, China

[*] Correspondence to Z.L. (zhliu@hku.hk) and P.A.W. (paul.wilson@noc.soton.ac.uk)

The Atlantic meridional overturning circulation (AMOC) exerts a major control on the global distribution of heat, dissolved oxygen, and carbon in the ocean. Yet, the timing and cause of the inception of this system and its evolution since the start of the Cenozoic Era 65 million years ago (Ma) remain highly uncertain. Here we present records of microbial source indicators based on glycerol dialkyl glycerol tetraether distributions from the Cenozoic Northwest Atlantic Ocean (~43–18 Ma) and use them to infer changes in AMOC-driven deep ocean oxygenation. At this location, oxygenation is strongly controlled by southwestward Deep Western Boundary Current transport of newly formed deep waters that feed AMOC. Our Eocene data show short-term high amplitude variability and an overall decrease in oxygenation of AMOC feed-waters culminating in especially poor ventilation between ~36.5 and ~34 Ma. AMOC-feed waters became better oxygenated upon initiation of Antarctic glaciation at the Eocene-Oligocene transition, ~34 Ma and were consistently well-ventilated from ~30 Ma. Our findings indicate a close association between the inception of Antarctic glaciation and AMOC and suggest that both vertical mixing and wind-driven upwelling in the Southern Ocean were key to fully establishing AMOC as an agent of deep ocean ventilation.

The Atlantic meridional overturning circulation (AMOC) exerts a strong control

on global climate and marine ecosystems, redistributing oceanic heat and salt, interacting with the atmosphere and ventilating the ocean interior. Modern AMOC is characterized by deep water formation in the North Atlantic and Southern Ocean, connected by cross-equatorial flows at the surface and at depth to form an interhemispheric circulation cell[1] (Fig. 1). To account for the energy required to sustain its modern strength, two physical mechanisms, vertical (diapycnal) mixing in the ocean interior and wind-driven upwelling in the Southern Ocean, are suggested to act together to drive AMOC, but their respective contributions are not straightforward to quantify[1].

The Cenozoic origins of AMOC and its possible relations with Southern Ocean gateway opening and Antarctic glaciation are far from well understood[2-16]. Proto-North Atlantic Deep Water, or Northern Component Water (NCW), is suggested to date from ~50 Ma[2] or around 40–38 Ma[3-5], but there exist many competing interpretations of the timing, cause and consequences of the onset of modern-like AMOC, characterized by the interhemispheric circulation cell[1]. Broadly speaking, these interpretations fall into two categories: those[6,7] that invoke its close association with the initiation of large-scale Antarctic glaciation at the Eocene-Oligocene transition (EOT), 34.44–33.65 Ma[17] and others[5,8,9] that suggest its earlier inception. The causal mechanisms invoked include Southern Ocean gateway opening[8,14], Antarctic glaciation[7], initiation of a strong Antarctic Circumpolar Current (ACC)[15], subsidence of the Greenland Scotland Ridge

(GSR)[5], and the closure of the Arctic-Atlantic seaway[16].

Most work on the early history of AMOC has focused on tracing water mass properties and flow using physicochemical approaches[3-6,8,9,12,15]. Here we take a novel approach, employing microbial source indicators, based on distributions of glycerol dialkyl glycerol tetraethers (GDGTs) (Extended Data Fig. 1), to infer water mass oxygenation history. Microbial source indicators, including methane index (MI)[18], ring index (ΔRI)[19], GDGT-0/cren[20], branched and isoprenoid tetraether index (BIT)[21], and the relative abundance of archaeol to caldarchaeol (ACE)[22] (Methods), typically used to evaluate non-thermal factors influencing the temperature proxy TEX_{86}[23], are employed here to infer microbial community changes, i.e., the contribution of other archaea/bacteria relative to the ubiquitous marine Thaumarchaeota[24].

Analysis of modern marine surface sediments and suspended particulate matter shows[25-28] that, although non-Thaumarhaeotal microbes can live in both oxic and anoxic environments, their relative abundance increases in anoxic environments (Methods). Hence, the relative abundance of non-Thaumarchaeota, particularly methanogenic and/or methanotrophic archaea, in geological samples, offers a means to evaluate the oxygenation status of past oceanic environments (Extended Data Fig. 2). Particularly low $\delta^{13}C$ values (< -40‰) of the alkyl moieties of GDGTs (Methods) can also indicate anaerobic oxidation of methane and methanogenesis in anoxic

environments[29,30]. Here we use this biomarker approach to study the oxygenation history of the North Atlantic Ocean and shed new light on the early evolution of AMOC (Fig. 1). Our data come from Integrated Ocean Drilling Program Site U1404 in the North Atlantic Ocean (Fig. 1). Site U1404 has a well-established chronology[31,32] and is located towards the base of J-Anomaly Ridge (water depth 4742 m), just downstream from the Labrador and Nordic seas where, today, deep ocean convection produces well oxygenated North Atlantic Deep Water that feeds AMOC[31,33,34].

GDGT source indicator records

Our records reveal pronounced changes in microbial community from ~43 to 18 Ma. MI values show an overall increase from the mid-Eocene to late Eocene and then decrease from ~34 Ma to ~30 Ma and there are marked superimposed fluctuations throughout the early part of our record until it stabilizes at low values (~0.2–0.3) from ~30 Ma (Fig. 2d). GDGT-0/cren, BIT, and ΔRI all display patterns of overall change similar to the MI record (Fig. 2b, 2c, Extended Data Fig. 3c). The ACE record shows maximum values between ~34 and 30 Ma (Extended Data Fig. 3d). Anomalously high index values, particularly in the late Eocene (~36.5–34 Ma), far exceed most values observed in modern marine settings where normal marine Thaumarchaeota are suggested to be the main producer of GDGTs (Extended Data Fig. 2, Methods). $\delta^{13}C$ values of the alkyl moieties of GDGTs decrease from the mid-Eocene to late Eocene

and earliest Oligocene, with lowest values around -35‰ to -40‰, and then return to high values around 30 Ma (Fig. 2e). Particularly low TEX_{86} values, around 0.2–0.4, also occurred in the late Eocene and early Oligocene (Extended Data Fig. 3b). Hence, all of our records consistently demonstrate maxima in non-Thaumarchaeota production in the latest Eocene, ~36.5–34 Ma.

The pattern of source indicator changes in our records resembles that of productivity change. Alkenone content[32] (a common primary productivity indicator), GDGT content, and shipboard total organic carbon and total nitrogen[31] all decreased from the mid-Eocene to late Eocene, increased from ~34 Ma to ~30 Ma, and were then maintained at relatively high levels from ~30 Ma (Extended Data Fig. 4). Alkenone concentrations[32] indicate a state shift to higher values around 34 Ma (Fig. 3c). The maximum in non-Thaumarchaeota production during the latest Eocene thus corresponds to minimum surface productivity between ~36.5 Ma and 34 Ma.

The long-term trend of increasing non-Thaumarchaeota contribution in our records corresponds to Eocene cooling (Fig. 3) and the marked shorter-term fluctuations in source indicator records before ~30 Ma also show this relationship with temperature. Intervals of increased non-Thaumarchaeota, represented by the higher GDGT-0/cren and MI values (Fig. 3d, 3e), generally correspond to intervals of cooler sea surface temperature[32] (SST) (Fig. 3b), lower alkenone concentration/surface productivity[32] (Fig.

3c), and lower (or zero) percentage of carbonate[31] (Fig. 3f), and vice versa.

A detailed history of early AMOC

Our biomarker records indicate that changes in the microbial community at our study site reflect seawater oxygenation in the deep North Atlantic Ocean. Organic carbon export cannot account for the intervals of deoxygenation documented by our records because these intervals are characterized by lower productivity than the more oxygenated intervals (Fig. 3). A sedimentary influence from seafloor methane seepage and hydrate dissociation on methanogenic and methanotrophic archaea must also be considered[29,30,35,36], but three observations suggest that methane seepage and/or hydrate dissociation does not exert a strong control on our records of microbial community variability in the open ocean conditions towards the base of J-Anomaly Ridge. First, carbonate content at our site is extremely low in most intervals with increased non-Thaumarchaeota (Fig. 3f) and, where measurable (34–34.5 Ma), carbonate $\delta^{13}C$ (data provided in Supplementary Table 1), far exceeds values influenced by methane discharge[18], indicating formation from sea water with little influence from methane seepage. Second, the sign of the relationship between deep water temperature and abundance of non-Thaumarchaeota that we document is opposite to that predicted by control through hydrate release: cooler ocean temperatures tend to stabilize hydrates[37] whereas we document higher non-Thaumarchaeota in cooler intervals (Fig. 3b). Third,

while glacioeustatic sea level fall-induced decrease in hydrostatic pressure can also trigger hydrate destabilization[38,39], our records show peak non-Thaumarchaeota production between ~36.5 and 34 Ma– before large ice sheets developed on Antarctica[40] (Fig. 3a), and reduced production after the EOT, contradicting a sea level control.

A striking feature in our records is the overall long-term reduction in ventilation of the deep Northwestern Atlantic Ocean toward the EOT, culminating in the pronounced oxygenation minimum between ~36.5 and 34 Ma. This observation contradicts suggestions[5,8,9] that a modern-like AMOC was initiated within this pre-EOT interval (Fig. 3). Our GDGT records indicate a later date for AMOC onset, consistent with interpretations of neodymium isotope (ε_{Nd}) records[6,12]. While there is some uncertainty over its precise timing, the long-term trend in oxygenation of AMOC-feed waters appears to have reversed at the EOT (Fig. 3d, 3e). The BIT and alkenone concentration records show relatively low amplitude fluctuations over the Eocene followed by major change at the EOT, suggesting weaker AMOC or NCW during the Eocene than after the EOT (Fig. 2c, 3c). These observations, together with the development, at about the same time, of temperature asymmetry between the North Atlantic and South Atlantic Ocean[32], suggest that the EOT marks the onset of more modern-like AMOC. Our records reveal diminishing variability in deep water oxygenation to ~30 Ma (Fig. 2) whereupon consistently well-ventilated conditions were

153 established, a date that corresponds to the suggested initiation of a well-developed
154 ACC[12] and four-layer ocean structure[15].

155 GDGT source indicator records available from other sites in the North Atlantic
156 Ocean are discontinuous and of low temporal resolution, but when considered together
157 they show comparable structure to our data (Extended Data Fig. 5), raising the
158 possibility of a major region-wide change in deep water oxygenation status at the EOT.
159 High-resolution work across the EOT from other sites is needed to test this
160 interpretation. The early AMOC history that we infer from these records of oxygenation
161 is consistent with other indications of enhanced deep-water formation in the earliest
162 Oligocene as summarized in ref[5] and does not necessarily contradict the existence of
163 NCW formation before the late Eocene[2-5]. In our records, ACE values peak between
164 ~34–30 Ma (Extended Data Fig. 3e), perhaps suggesting a community shift in seawater
165 from a dominance of methanogenic and methanotrophic archaea to halophilic archaea,
166 then to the normal marine Thaumarchaeota and thus improved deep ocean oxygenation
167 status. Together with the large fluctuations by ~30 Ma recorded in other GDGT records
168 (Fig. 2, Extended Data Fig. 3), our interpretation of these records is consistent with the
169 development of four-layer ocean structure[15].

170 Anomalously low $\delta^{13}C$ in benthic foraminiferal calcite is reported[3] for the late
171 Eocene North Atlantic (Fig. 4c) and interpreted to indicate the influence of nutrient-rich

172 water sourced from the Arctic Ocean[9] or enhanced southern-sourced intermediate
173 water[5,15], and early onset of AMOC before the EOT[5,9]. An alternative explanation for
174 these low benthic $\delta^{13}C$ values is that they indicate nutrient accumulation under stratified
175 conditions[9], similar to those found today in the North Pacific Ocean. This interpretation
176 is supported by the extremely low surface productivity over the late Eocene in our
177 records (Fig. 4, Extended Data Fig. 4). Traditionally, the increasing trend to more
178 radiogenic (higher ε_{Nd}) in Southern Ocean ε_{Nd} records[6,12] over the Eocene is interpreted
179 as increased influence of Pacific sourced waters[6]. However, Eocene reduction of NCW
180 can also explain this signal (Fig. 4). Regardless, lower values (less radiogenic) in the
181 ε_{Nd} records from the EOT onwards in the Southern Ocean (Fig. 4c) are consistent with
182 our interpretation of invigoration of AMOC and deep ocean oxygenation from ~34 Ma.
183 Furthermore, North Pacific ε_{Nd} records indicate a gradual shutdown of the deep water
184 sinking from ~36 Ma onwards, which may reflect competition[41] with the North Atlantic
185 to fill the deep ocean once AMOC was established.

186 **What drove changes in early AMOC strength?**

187 The overall reduction in NCW through Eocene time and strengthening of AMOC
188 at the EOT implied by our data are not readily explained by tectonic control. A shallow
189 connection through the Drake Passage at ~41 Ma[10] is suggested to have allowed the
190 development of proto-ACC[11]. The deep Tasmanian Gateway opened at 33.5 ± 1.5 Ma

and a strong, fully developed ACC is suggested to have initiated ~30 Ma when it became aligned with the westerly winds[12,13]. In the North Atlantic, accelerated subsidence of the GSR[5] and the Arctic-Atlantic seaway closure[16] are proposed to have occurred around ~37–34 Ma, although their precise timing remains difficult to constrain[42-46]. Southern Ocean gateway opening[14], proto-ACC formation[15], and GSR subsidence[5] are all suggested to have promoted NCW formation during the late Eocene, inconsistent with our results (Fig. 4). Increased Arctic freshwater input[16] due to Atlantic Basin expansion could have contributed to the overall Eocene reduction in NCW implied by our records. However, this mechanism cannot readily explain the marked short-term fluctuations in which increased NCW production is indicated for warmer intervals, because model simulations indicate the opposite relationship[46]. Further, we see no particular indication of AMOC disruption in our records during the early Miocene (Fig. 2) when the Arctic gateway reopened[45]. Meanwhile, the close association between Eocene NCW production and the surface ocean conditions that we document (Fig. 3) calls for a temperature control on the strength of vertical mixing in the North Atlantic Ocean. Intervals of enhanced ventilation of AMOC-feed waters correspond to warmer conditions on various timescales during the Eocene[47] and Pleistocene[48], supporting this interpretation.

The onset of better ventilated AMOC-feed waters at the EOT in our records (Fig.

4) points to Antarctic glaciation-driven ocean circulation change[7] following tectonic preconditioning of the Southern[12] and North Atlantic[42,43] oceans. Our records suggest that AMOC-feed waters became consistently well-ventilated from ~30 Ma when the ACC is suggested to have first aligned with the westerly winds[12]. Although our records, together with other data sets[12,15] (Fig. 4), support a stabilization role for the ACC on AMOC, the relationship between the ACC and AMOC appears to be model-dependent in numerical simulations[8,11,49,50]. Hence, the physical mechanisms that stabilized AMOC remain to be identified, and some role for North Atlantic tectonics cannot be ruled out.

Our GDGT source indicator records reveal a detailed history of ventilation in the North Atlantic Ocean between ~43 Ma and 18 Ma. We document an overall reduction of Eocene NCW ventilation controlled by temperature changes, the onset of modern-like AMOC at the EOT likely triggered by Antarctic glaciation, and consistently well-ventilated conditions from ~30 Ma when the ACC became well-developed. Our data, indicating a weak form of Eocene NCW and then the development of modern-like AMOC closely associated with Antarctic glaciation and a well-developed ACC, call into question suggestions that a strong AMOC initiated well before the EOT and lend support to the proposed importance of both vertical mixing and Southern Ocean wind-driven upwelling for sustaining modern AMOC[1].

Acknowledgments

This research used samples provided by the Integrated Ocean Drilling Program (IODP), which is sponsored by the US National Science Foundation and participating countries under management of Joint Oceanographic Institutions, Inc. We thank the scientists and supporting staff of IODP Expedition 342, IODP for providing samples for this study, IODP China office for additional support, and Ronnakrit Rattanasriampaipong (Texas A&M University) and two anonymous reviewers for constructive comments. This research was supported by Chinese Academy of Sciences (XDB40000000) (to W.L. & Z.L.), Hong Kong Research Grant Council Grant 17305019 and 17303614 (to Z.L.), UK Natural Environment Research Council (NERC) Grant NE/L007452/1 (to S.M.B), NERC Grant NE/K014137/1 (to P.A.W.), a Royal Society Wolfson award (to P.A.W.), the National Natural Science Foundation of China 42122021 (to H.W.) and 42273059 (to Y.Z.), and the Youth Innovation Promotion Association CAS 2019403 (to H.W.).

Author Contributions Statement

P.A.W. and Z.L. participated in IODP Expedition 342 in seagoing capacities. Z.L., W.L., S.M.B and P.A.W. conceived the idea of using GDGT source indicators to infer early AMOC history. H.W., W.L., H.L., Y.Z., Y.L. and Y.H. performed data analysis. Z.L. and P.A.W. led the writing of the manuscript with intellectual contributions from all co-authors.

Competing Interests Statement

The authors declare no competing interests.

Figure Captions

Figure 1 | Site locations and modern dissolved oxygen level in the Atlantic Basin. **a**, Site locations of the records included in this study, superimposed on mean annual surface temperature field. **b**, Latitudinal cross section of modern dissolved oxygen level approximately along the indicated NADW path (blue line) in **a**. Map template made with Ocean Data View (https://odv.awi.de/) and modern oxygen data from https://www.ncei.noaa.gov/sites/default/files/2022-06/woa18_vol3.pdf. NAC, North Atlantic Current; ACC, Antarctic Circumpolar Current; NADW, North Atlantic Deep Water; AAIW, Antarctic Intermediate Water; AABW, Antarctic Bottom Water; GSR: Greenland-Scotland Ridge.

Figure 2 | Mid-Eocene to early Miocene GDGT records from U1404 in the North Atlantic. **a**, Global benthic $\delta^{18}O$ record[3]. **b**, GDGT-0/cren. **c**, BIT (branched and isoprenoid tetraether index). **d**, MI (methane index). **e**, $\delta^{13}C$ values of the alkyl moieties of GDGTs with chemical structures indicated. See Methods for definitions of GDGT source indicators and compound names. Interval of elevated index values at ~36.5–34 Ma highlighted. Y-axis inverted in **b**–**d** to indicate better oxygenation upward. Age error

bars (one standard deviation) in **e** indicates $\delta^{13}C$ analysis made from combined samples (n = 6, Methods). The Eocene-Oligocene boundary (EOB, 33.9 Ma) indicated for reference.

Figure 3 | Detailed view of changes in microbial community and association with surface conditions at U1404. a, Relative sea level changes[40]. **b**, Sea surface temperature (SST), with empty circles indicating estimates associated with relatively low alkenone content and data points disconnected for intervals with unreported SST due to even lower content[32]. **c**, Alkenone concentration (C_{37})[32]. **d**, GDGT-0/cren. **e**, MI (methane index). **f**, Shipboard[31] and lab (circles)[32] measurements of carbonate percentage (%$CaCO_3$). Peak non-Thaumarchaeota production at ~36.5–34 Ma highlighted with light green bar and intervals of warm SST and increased surface productivity, generally corresponding to reduced non-Thaumarchaeota production, indicated by yellow bars. EOB the same as Fig. 2.

Figure 4 | Representative early AMOC records. a, Global benthic $\delta^{18}O$ record[3]. **b**, Benthic $\delta^{13}C$ records (black, global compilation)[3,4,9,15], with particularly low late Eocene $\delta^{13}C$ values in the North Atlantic (Site 647). **c**, ε_{Nd} records[6,12]. **d**, Alkenone concentration[32], and **e**, MI (methane index) at U1404. In **b** and **c**, data points for relatively low-resolution or discontinuous records were disconnected. Minima in Northern Component Water (NCW) production at ~36.5–34 Ma (light green bar) and a

state shift after (red bar, indicated by alkenone concentration) possibly constrain modern-like AMOC onset at the Eocene-Oligocene transition (EOT, 34.44–33.65 Ma[17]). EOB the same as Fig. 2.

References

1. Kuhlbrodt, T. *et al*. On the driving processes of the Atlantic meridional overturning circulation. *Rev. Geophys.* **45**, RG2001 (2007).

2. Hohbein, M. W., Sexton, P. F. & Cartwright, J. A. Onset of North Atlantic Deep Water production coincident with inception of the Cenozoic global cooling trend. *Geology* **40**, 255–258 (2012).

3. Cramer, B. S., Toggweiler, J. R., Wright, J. D., Katz, M. E. & Miller, K. G. Ocean overturning since the Late Cretaceous: Inferences from a new benthic foraminiferal isotope compilation. *Paleoceanography* **24**, PA4216 (2009).

4. Borrelli, C., Cramer, B. S. & Katz, M. E. Bipolar Atlantic deepwater circulation in the middle-late Eocene: Effects of Southern Ocean gateway openings. *Paleoceanography* **29**, 308–327 (2014).

5. Abelson, M. & Erez, L. The onset of modern-like Atlantic meridional overturning circulation at the Eocene-Oligocene transition: Evidence, causes, and possible implications for global cooling. *Geochem. Geophys. Geosyst.* **18**, 2177–2199

(2017).

6. Via, R. K. & Thomas, D. J. Evolution of Atlantic thermohaline circulation: Early Oligocene onset of deep-water production in the North Atlantic. *Geology* **34**, 441–444 (2006).

7. Goldner, A., Herold, N. & Huber, M. Antarctic glaciation caused ocean circulation changes at the Eocene–Oligocene transition. *Nature* **511**, 574–577 (2014).

8. Elsworth, G., Galbraith, E. Halverson, G. & Yang, S. Enhanced weathering and CO_2 drawdown caused by latest Eocene strengthening of the Atlantic meridional overturning circulation. *Nat. Geosci.* **10**, 213–216 (2017).

9. Coxall, H. K. *et al.* Export of nutrient rich Northern Component Water preceded early Oligocene Antarctic glaciation. *Nat. Geosci.* **11**, 190–196 (2018).

10. Livermore, R., Hillenbrand, C. D., Meredith, M. & Eagles, G. Drake Passage and Cenozoic climate: An open and shut case? *Geochem. Geophys. Geosyst.* **8**, Q01005 (2007).

11. Sijp, W. P., England, M. H. & Huber, M. Effect of the deepening of the Tasman Gateway on the global ocean. *Paleoceanography* **26**, PA4207 (2011).

12. Scher, H. D. *et al*. Onset of Antarctic Circumpolar Current 30 million years ago as Tasmanian Gateway aligned with westerlies. *Nature* **523**, 580–583 (2015).

13. Hill, D. J. *et al.* Paleogeographic controls on the onset of the Antarctic circumpolar current. *Geophys. Res. Lett.* **40**, 5199-5204 (2013).

14. Toggweiler, J. R. & Bjornsson, H. Drake passage and palaeoclimate. *J. Quat. Sci.* **15**, 319–328 (2000).

15. Katz, M. E. *et al*. Impact of Antarctic circumpolar current development on Late Paleogene ocean structure. *Science* **332**, 1076–1079 (2011).

16. Hutchinson, D. K. *et al.* Arctic closure as a trigger for Atlantic overturning at the Eocene-Oligocene Transition. *Nat. Commun.* **10**, 3797 (2019).

17. Hutchison, D. K. *et al.* The Eocene–Oligocene transition: a review of marine and terrestrial proxy data, models and model–data comparisons. *Clim. Past* **17**, 269–315 (2021).

18. Zhang, Y. G. *et al*. Methane Index: A tetraether archaeal lipid biomarker indicator for detecting the instability of marine gas hydrates. *Earth Planet. Sci. Lett.* **307**, 525–534 (2011).

19. Zhang, Y. G., Pagani, M. & Wang, Z. Ring Index: A new strategy to evaluate the integrity of TEX_{86} paleothermometry. *Paleoceanography* **31**, 220–232 (2016).

20. Blaga, C. I., Reichart, G.-J., Heiri, O. & Sinninghe Damsté, J. S. Tetraether membrane lipid distributions in water-column particulate matter and sediments: a

340 study of 47 European lakes along a north–south transect. *J. Paleolimnol.* **41**, 523–
341 540 (2009).

342 21. Hopmans, E. C. *et al.* A novel proxy for terrestrial organic matter in sediments based
343 on branched and isoprenoid tetraether lipids. *Earth Planet. Sci. Lett.* **224**, 107–116
344 (2004).

345 22. Turich, C. & Freeman, K. H. Archaeal lipids record paleosalinity in hypersaline
346 systems. *Org. Geochem.* **42**, 1147–1157 (2011).

347 23. Schouten, S., Hopmans, E. C., Schefuß, E. & Sinninghe Damsté, J. S. Distributional
348 variations in marine crenarchaeotal membrane lipids: a new tool for reconstructing
349 ancient sea water temperatures. *Earth Planet. Sci. Lett.* **204**, 265–274 (2002).

350 24. Sinninghe Damsté, J. S., Schouten, S., Hopmans, E. C., Van Duin, A. C. &
351 Geenevasen, J. A. Crenarchaeol: the characteristic core glycerol dibiphytanyl
352 glycerol tetraether membrane lipid of cosmopolitan pelagic crenarchaeota. *J. Lipid*
353 *Res.* **43**, 1641–1651 (2002).

354 25. Kim, J.-H. *et al.* New indices and calibrations derived from the distribution of
355 crenarchaeal isoprenoid tetraether lipids: Implications for past sea surface
356 temperature reconstructions. *Geochim. Cosmochim. Acta* **74**, 4639–4654 (2010).

357 26. Ho, S. L. *et al.* Appraisal of TEX_{86} and TEX_{86}^{L} thermometries in subpolar and polar

regions. *Geochim. Cosmochim. Acta* **131**, 213–226 (2014).

27. Zhu, C. *et al.* Stratification of archaeal membrane lipids in the ocean and implications for adaptation and chemotaxonomy of planktonic archaea. *Environ. Microbiol.***18**, 4324–4336 (2016).

28. Rattanasriampaipong, R. *et al.* Archaeal lipids trace ecology and evolution of marine ammonia-oxidizing archaea. *Proc. Natl Acad. Sci. USA* **119**, e2123193119, (2022).

29. Pancost R. D. *et al.* Biomarker evidence for widespread anaerobic methane oxidation in Mediterranean sediments by a consortium of methanogenic archaea and bacteria. *Appl. Environ. Microbiol.* **66**, 1126–1132 (2000).

30. Blumenberg, M., Seifert, R., Reitner, J., Pape, T. & Michaelis, W. Membrane lipid patterns typify distinct anaerobic methanotrophic consortia. *Proc. Natl Acad. Sci. USA* **101**, 11111–11116 (2004).

31. Norris, R. D. *et al*. Site U1404. In Norris, R. D., Wilson, P. A., Blum, P. & the Expedition 342 Scientists, *Proc. IODP*, **342** (2014): College Station, TX (Integrated Ocean Drilling Program).

32. Liu, Z. *et al*. Transient temperature asymmetry between hemispheres in the Palaeogene Atlantic Ocean. *Nat. Geosci.* **11**, 656–660 (2018).

33. Keeling, R. F., Körtzinger, A. & Gruber, N. Ocean deoxygenation in a warming world. *Annu. Rev. Mar. Sci.* **2**,199–229 (2010).

34. Tjiputra, J. F. *et al.* Mechanisms and early detections of multidecadal oxygen changes in the interior subpolar North Atlantic. *Geophys. Res. Lett.* **45**, 4218–4229 (2018).

35. Elvert, M., Suess, E., Greinert, J. & Whiticar, M. J. Archaea mediating anaerobic methane oxidation in deep-sea sediments at cold seeps of the eastern Aleutian subduction zone. *Org. Geochem.* **31**, 1175–1187 (2000).

36. Skarke, A., Ruppel, C., Kodis, M., Brothers, D. & Lobecker, E. Widespread methane leakage from the sea floor on the northern US Atlantic margin. *Nat. Geosci.* **7**, 657–661 (2014).

37. Ferré, B. *et al.* Reduced methane seepage from Arctic sediments during cold bottom-water conditions. *Nat. Geosci.* **13**, 144–148 (2020).

38. Watanabe, Y., Nakai, S., Hiruta, A., Matsumoto, R. & Yoshida, K. U–Th dating of carbonate nodules from methane seeps off Joetsu, Eastern Margin of Japan Sea. *Earth Planet. Sci. Lett.* **272**, 89–96 (2008).

39. Kim, B. & Zhang, Y. G. Methane hydrate dissociation across the Oligocene-Miocene boundary. *Nat. Geosci.* **15**, 203–209 (2022).

40. Miller, K. G. *et al.* Cenozoic sea-level and cryospheric evolution from deep-sea geochemical and continental margin records. *Sci. Adv.* **6**, eaaz1346 (2020).

41. McKinley, C. C., Thomas, D. J., LeVay, L. J. & Rolewicz, Z. Nd isotopic structure of the Pacific Ocean 40–10 Ma, and evidence for the reorganization of deep North Pacific Ocean circulation between 36 and 25 Ma. *Earth Planet. Sci. Lett.* **521**, 139–149 (2019).

42. Wright, J. D. & Miller, K. G. Control of North Atlantic Deep Water Circulation by the Greenland-Scotland Ridge. *Paleoceanography* **11**, 157–170 (1996).

43. Parnell-Turner, R. *et al.* A continuous 55-million-year record of transient mantle plume activity beneath Iceland. *Nat. Geosci.* **7**, 914–919 (2014).

44. Hegewald, A. & Jokat, W. Relative sea level variations in the Chukchi region—Arctic Ocean—since the late Eocene. *Geophys. Res. Lett.* **40**, 803–807 (2013).

45. Jakobsson, M. *et al.* The early Miocene onset of a ventilated circulation regime in the Arctic Ocean. *Nature* **447**, 986–990 (2007).

46. Stärz, M., Jokat, W., Knorr, G. & Lohmann, G. Threshold in North Atlantic–Arctic Ocean circulation controlled by the subsidence of the Greenland–Scotland Ridge. *Nat. Commun.* **8**, 15681 (2017).

47. Sexton, P. F. *et al.* Eocene global warming events driven by ventilation of oceanic

412 dissolved organic carbon. *Nature* **471**, 349–352 (2011).

413 48. Thomas, N. C., Bradbury, H. J. & Hodell, D. A. Changes in North Atlantic deep-
414 water oxygenation across the Middle Pleistocene Transition. *Science* **377**, 654–659
415 (2022).

416 49. Marshall, J. & Speer, K. Closure of the meridional overturning circulation through
417 Southern Ocean upwelling. *Nat. Geosci.* **5**, 171–180 (2012).

418 50. Toumoulin, A. *et al.* Quantifying the effect of the Drake Passage opening on the
419 Eocene Ocean. *Paleoceanogr. Paleoclimatol.* **35**, e2020PA003889 (2020).

420

421 **Methods**

422 **Materials.** Materials came from IODP Expedition 342 Site U1404 (40.00 °N, 51.60 °W,
423 water depth 4742 m)[31] (Fig. 1). Age control points based on shipboard planktonic
424 foraminifers, radiolarians, calcareous nannofossils, and paleomagnetics were used to
425 construct its chronology[31], which was independently checked by the $\delta^{18}O$ stratigraphy
426 at the EOT section[32]. Alkenones in ~360 sediment samples, at a sampling resolution of
427 ~60-80 kyr, were analyzed previously[32]. Glycerol dialkyl glycerol tetraethers (GDGTs)
428 were analyzed from the same sample set here. A small set of samples (25) were selected
429 for $\delta^{13}C$ analysis of the alkyl moieties of GDGTs.

GDGT analysis. Sediments were freeze-dried, ground, and extracted with a Dionex Accelerated Solvent Extractor (ASE300). We performed basic hydrolysis on the extracted lipids and then separated them into 3 compound classes using silica column chromatography. The alkenone fraction was analyzed on an Agilent 7890 gas chromatograph (GC)[32]. Analysis of microbial ether lipids was described previously[51]. Briefly, the methanol fraction was dried under N_2, re-dissolved in *n*-hexane/isopropanol (99:1, v/v) and filtered through a 0.22 μm PTFE filter after adding a known amount of C_{46} internal standard[52]. Archaeal and bacterial ether lipids were analyzed by a Shimadzu LC-MS 8030 high-performance liquid chromatography with atmospheric pressure chemical ionization–mass spectrometry at the Institute of Earth Environment, Chinese Academy of Sciences[53]. Separation of GDGTs was achieved with an Inertsil CN-3 column (250 mm×4.6 mm, 3μm; GL Sciences Inc.) at 40 ˚C using *n*-hexane:isopropanol (9:1, v/v) and *n*-hexane as elutes for pump A and pump B, respectively. MS scanning was performed in selected ion monitoring (SIM) mode that targeted specific $[M+H]^+$ ions (archaeol, 653.6; isoprenoid GDGTs: caldarchaeol/GDGT-0, 1302.3; GDGT-1, 1300.3; GDGT-2, 1298.3; GDGT-3, 1296.3; crenarchaeol (cren), 1292.3; crenarchaeol′ (cren′), 1292.3; branched GDGTs: IIIa, 1050; IIIb, 1048; IIIc, 1046; IIa, 1036; IIb, 1034; IIc, 1032; Ia, 1022; Ib, 1020; Ic, 1018) (Extended Data Fig. 1). The concentrations of GDGTs were quantified under the assumption that their ionization efficiency is the

449 same as that of the internal standard, while archaeol has a 10-times ionization efficiency
450 on our instrument[53].

451 **GDGT source indicators.** The microbial source indicators, methane index (MI)[18], ring
452 index (ΔRI)[19], GDGT-0/cren[20], branched and isoprenoid tetraether index (BIT)[21], and
453 the relative abundance of archaeol to caldarchaeol (ACE)[22], and the temperature proxy
454 TEX_{86}[23], are calculated as follows:

455 MI = (GDGT-1+GDGT-2+GDGT-3)/(GDGT-1+GDGT-2+GDGT-3+cren+cren′)

456 RI = 1*GDGT-1+2*GDGT-2+3*GDGT-3+4*cren+4*cren′

457 $\Delta RI = RI_{TEX} - RI$

458 BIT = (IIIa+IIa+Ia)/(cren+IIIa+IIa+Ia)

459 ACE = archaeol/(archaeol+GDGT-0) *100

460 TEX_{86} = (GDGT-2+GDGT-3+cren′)/(GDGT-1+GDGT-2+GDGT-3+cren′)

461 whereas RI_{TEX} is the theoretical RI value inferred from the RI/TEX_{86} relationship based
462 on modern core top results[19]: $RI_{TEX} = -0.77*TEX_{86} + 3.32*(TEX_{86})^2 + 1.59$, and based
463 on compilation of modern SPM dataset[28]: $RI_{TEX} = 0.98*TEX_{86} + 1.07*(TEX_{86})^2 + 1.41$.
464 Estimated analytical error from repeated analyses of our laboratory standards is 0.01
465 unit for TEX_{86} and generally within 5% of their respective values for those source

466 indicators.

467 MI indicates contribution from methanotrophic archaea[18] and ΔRI monitors non-
468 thermal factors influencing the TEX_{86} index[19] as utilization of this temperature proxy
469 assumes that isoprenoid GDGTs are mainly produced by the normal marine
470 Thaumarchaeota[54]. GDGT-0/cren, which is essentially equivalent to %cren[55] as the two
471 are generally the most abundant isoprenoid GDGTs, detects methanogenic archaea[20].
472 BIT was originally proposed to indicate terrestrial input[21], but branched GDGTs could
473 also be produced *in situ* from likely marine non-Thaumarchaeota[56-59]. ACE, proposed
474 to indicate water salinity[22,53], reflects the contribution from halophilic archaea. Hence,
475 although they are proposed to reflect various environmental factors in particular settings,
476 all those source indicators follow the same fundamental principle, the contribution of
477 other archaea/bacteria relative to the normal marine Thaumarchaeota, which this study
478 is based on. We also used additional GDGT-based indicators, IIIa/IIa[60] for further
479 evaluation of terrestrial input and GDGT-2/GDGT-3[28,61] for supporting deep-water
480 GDGTs contributed to the sedimentary pool.

481 The relative abundance of non-Thaumarchaeotal microbes, methanogenic and/or
482 methanotrophic archaea in particular, could then be indicative of anoxic conditions. The
483 stratification of microbial membrane lipids in modern anoxic marine environments, the
484 euxinic Black Sea basin particularly, have been well demonstrated[29,58,59,62-66]. GDGT-

485 producing community structure associated with redox conditions is also reported in
486 deep water lakes[67-71], and some source indicators are applied to reconstruct stratification
487 status of Pliocene coastal waters[51]. The cut-off values to indicate substantial non-
488 Thaumarchaeota contribution in marine settings are 0.3 (MI)[18], 0.3 (ΔRI)[19], 2 (GDGT-
489 0/cren)[20], 0.4 (BIT)[21] and ~10% (ACE) respectively (Extended Data Fig. 2).

490 We note that anoxic conditions do not result in particularly high MI values in some
491 regions of modern oxygen minimum zones (OMZs) or could not be recorded in the
492 Black Sea sediments[27], due to possible complex mechanisms[64,65]. Yet, the ACE values
493 from OMZ SPM are comparably high as those of the Black Sea SPM[27] (Extended Data
494 Fig. 2d). It is also plausible that OMZs typically occur at upper subsurface, ~500 m
495 water depth, in contrast to the overall low oxygenation throughout the subsurface water
496 column in the Black Sea and subpolar North Pacific. However, for our study site, the
497 GDGT-2/GDGT-3[28,61] and IIIa/IIa[60] records indicate substantial deep-water GDGTs
498 contributed to the sedimentary pool, with little terrestrial influence (Extended Data Fig.
499 3e, 3f). Hence, the abnormally high MI values, together with other source indicators,
500 could be confidently linked to anoxic environments in this study as MI is a powerful
501 indicator for methanogenic archaea. This interpretation is also consistent with the
502 general notion of increased abundance of non-Thaumarchaeota, methanogenic and/or
503 methanotrophic archaea in particular, toward anoxic environments, based on numerous

modern studies. Perhaps due to the special oceanic setting in the North Atlantic Ocean over the study period, drastic microbial community changes allow all source indicators to perform consistently (Fig. 2, Extended Data Fig. 3).

GDGT $\delta^{13}C$ analysis. The alkyl moieties of the GDGTs were released from the cleavage of ether bonds based on the reported procedure[72]. Initially, the extract was treated with an excess of BBr_3 in dichloromethane (DCM, HPLC grade) for 2 h at 70 °C under an atmosphere of high purity argon (99.999%). The resulting alkyl bromides were converted to corresponding hydrocarbons by reaction with a slight excess of $Li(C_2H_5)_3BH$ for 2 h at 70 °C in tetrahydrofuran, also under argon. After quenching the reaction using deionized water, the products were extracted with DCM and the hydrocarbons were purified by a silica gel column, eluting with hexane. The hexane elute was carefully dried under a N_2 stream for further analysis. As GDGT content was extremely low at ~38–30 Ma (Extended Data Fig. 4), 6 consecutive samples were combined into one and 8 combined samples were made for $\delta^{13}C$ analysis, indicated by the age error bars (one standard deviation) shown in Fig. 2e. For this reason, the $\delta^{13}C$ values at ~37.5–32.8 Ma likely represent mean conditions, unable to capture the marked variability within this interval as suggested by GDGT indicators, while the generally similar temporal trends in $\delta^{13}C$ and GDGT indices support our use of those indices as oxygenation indicator (Fig. 2).

523 Individual GDGT-derived alkanes were quantified with a HP 6890 GC at the
524 Institute of Earth Environment, Chinese Academy of Sciences. A capillary column (HP-
525 1 MS, 60 m, 0.32 mm inner diameter, 0.25 μm film thickness) was used with He (1.3
526 ml/min) as the carrier gas. The GC column was held at 60 °C for 1 min and then
527 programmed to 320 °C (held 45 min) at 30 °C /min.

528 $\delta^{13}C$ analysis of the alkanes was performed using GC-thermal conversion-isotope
529 ratio mass spectrometry. A Thermo Trace Ultra GC was used along with a high
530 temperature pyrolysis unit connected online to a Thermo Delta V Advantage isotope
531 ratio mass spectrometer. Individual compounds were pyrolyzed at 1450 °C to CO_2,
532 which was introduced into the mass spectrometer. The temperature program and GC
533 column were identical to those used for GC analysis. Reproducibility and accuracy were
534 evaluated using standards containing five *n*-alkanes (C_{21}, C_{25}, C_{27}, C_{29}, C_{33}) between
535 every four measurements. Based on this, the internal precision of the measurements was
536 determined to be ± 0.3‰. An internal standard (*n*-C_{36} alkane) was also applied to
537 examine the precision of quantitative analysis. Due to the low GDGT content, only
538 acyclic biphytane (Bp-0) and monocyclic biphytane (Bp-1) from isoprenoid GDGTs[30]
539 and dimethyloctacosanes (a) and trimethyloctacosanes (b) from branched GDGTs[67]
540 yield meaningful measurements (Fig. 2e). As some biphytane response is relatively low,
541 we estimate that those $\delta^{13}C$ measurements are associated with slightly larger errors,

around ± 1.0‰.

Additional data sources of GDGTs[73-76], $\delta^{13}C$[77,78] and ε_{Nd}[79,80] records were used in figure presentation.

Data availability. We declare that the new data that support the findings of this study are available in Supplementary Table. All new data associated with the paper can also be accessed at https://doi.org/10.6084/m9.figshare.21922107.

Methods-only References

51. Wang, M. *et al.* Late Miocene-Pliocene Asian summer monsoon variability linked to both tropical Pacific temperature and Walker Circulation. *Earth Planet. Sci. Lett.* **561**, 116823 (2021).

52. Schouten, S., Huguet, C., Hopmans, E. C., Kienhuis, M. V. & Sinninghe Damsté, J. S. Analytical methodology for TEX_{86} paleothermometry by high-performance liquid chromatography/atmospheric pressure chemical ionization-mass spectrometry. *Anal. Chem.* **79**, 2940–2944 (2007).

53. Wang, H. *et al.* Assessing the ratio of archaeol to caldarchaeol as a salinity proxy in highland lakes on the northeastern Qinghai-Tibetan Plateau. *Org. Geochem.* **54**, 69–77 (2013).

559 54. Schouten, S., Hopmans, E. C. & Sinninghe Damsté, J. S. The organic geochemistry
560 of glycerol dialkyl glycerol tetraether lipids: A review. *Org. Geochem.* **54**, 19–61
561 (2013).

562 55. Wang, H. *et al.* Water depth affecting thaumarchaeol production in Lake Qinghai,
563 northeastern Qinghai-Tibetan plateau: Implications for paleo lake levels. *Chem.*
564 *Geol.* **368**, 76–84 (2014).

565 56. Peterse, F. *et al.* Constraints on the application of the MBT/CBT palaeothermometer
566 at high latitude environments (Svalbard, Norway). *Org. Geochem.* **40**, 692–699,
567 (2009) .

568 57. Weijers, J. W. H., Schefuß, E., Kim, J.-H., Sinninghe Damsté, J. S. & Schouten, S.
569 Constraints on the sources of branched tetraether membrane lipids in distal marine
570 sediments. *Org. Geochem.* **72**, 14–22 (2014).

571 58. Liu, X.-L., Zhu, C., Wakeham, S. G. & Hinrichs, K.-U. In situ production of
572 branched glycerol dialkyl glycerol tetraethers in anoxic marine water columns. *Mar.*
573 *Chem.* **166**, 1–8 (2014).

574 59. Xie, S., Liu, X.-L., Schubotz, F., Wakeham, S. G. & Hinrichs, K.-U. Distribution of
575 glycerol ether lipids in the oxygen minimum zone of the Eastern Tropical North
576 Pacific Ocean. *Org. Geochem.* **71**, 60–71 (2014).

60. Xiao, W. *et al.* Ubiquitous production of branched glycerol dialkyl glycerol tetraethers (brGDGTs) in global marine environments: a new source indicator for brGDGTs. *Biogeosci.* **13**, 5883–5894 (2016).

61. Taylor, K. W. R., Huber, M., Hollis, C. J., Hernandez-Sanchez, M. T. & Pancost, R. D. Re-evaluating modern and Palaeogene GDGT distributions: Implications for SST reconstructions. *Glob. Planet. Change* **108**, 158–174, (2013).

62. Pitcher, A. *et al.* Niche segregation of ammonia-oxidizing archaea and anammox bacteria in the Arabian Sea oxygen minimum zone. *ISME J.* **5**, 1896–1904 (2011).

63. Schouten, S. *et al.* Intact polar and core glycerol dibiphytanyl glycerol tetraether lipids in the Arabian Sea oxygen minimum zone: I. Selective preservation and degradation in the water column and consequences for the TEX_{86}. *Geochim. Cosmochim. Acta* **98**, 228–243 (2012).

64. Wakeham, S. G., Lewis, C. M., Hopmans, E. C., Schouten, S. & Sinninghe Damsté, J. S. Archaea mediate anaerobic oxidation of methane in deep euxinic waters of the Black Sea. *Geochim. Cosmochim. Acta* **67**, 1359–1374 (2003).

65. Wakeham, S. G., Hopmans, E. C., Schouten, S. & Sinninghe Damsté, J. S. Archaeal lipids and anaerobic oxidation of methane in euxinic water columns: a comparative study of the Black Sea and Cariaco Basin. *Chem. Geol.* **205**, 427–442 (2004).

595 66. Wakeham, S. G. *et al.* Microbial ecology of the stratified water column of the Black
596 Sea as revealed by a comprehensive biomarker study. *Org. Geochem.* **38**, 2070–
597 2097 (2007).

598 67. Weber, Y. *et al.* Redox-dependent niche differentiation provides evidence for
599 multiple bacterial sources of glycerol tetraether lipids in lakes. *Proc. Natl Acad. Sci.*
600 *USA* **115**, 10926–10931 (2018).

601 68. Wu, J. *et al.* Variaitons in dossolved O_2 in a Chinese lake drive changes in microbial
602 communities and impact sedimentary GDGT distributions. *Chem. Geol.* **579**,
603 120348 (2021).

604 69. Schouten, S., Rijpstra, W. I. C., Durisch-Kaiser, E., Schubert, C. J. & Sinninghe
605 Damsté, J. S. Distribution of glycerol dialkyl glycerol tetraether lipids in the water
606 column of Lake Tanganyika. *Org. Geochem.* **53**, 34–37 (2012).

607 70. Baxter, A. J. *et al.* Seasonal and multi-annual variation in the abundance of
608 isoprenoid GDGT membrane lipids and their producers in the water column of a
609 meromictic equatorial crater lake (Lake Chala, East Africa). *Quat. Sci. Rev.* **273**,
610 107263 (2021).

611 71. Sinninghe Damsté, J. S., Weber, Y., Zopfi, J., Lehmann, M. F. & Niemann, H.
612 Distributions and sources of isoprenoidal GDGTs in Lake Lugano and other central

European (peri-)alpine lakes: Lessons for their use as paleotemperature proxies. *Quat. Sci. Rev.* **277**, 107352 (2022).

72. Summons, R. E., Franzmann, P. D. & Nichols, P. D. Carbon isotopic fractionation associated with methylotrophic methanogenesis. *Org. Geochem.* **28**, 465–476 (1998).

73. Inglis, G. N. *et al.*, Descent toward the Icehouse: Eocene sea surface cooling inferred from GDGT distributions. *Paleoceanography* **30**, 1000–1020 (2015).

74. Śliwińska, K. K., Mets, A. & Schouten, S. In Norris, R.D., Wilson, P.A., Blum, P. & the Expedition 342 Scientists, *Proc. IODP*, **342** (2017): College Station, TX (Integrated Ocean Drilling Program).

75. Guitián, J. *et al.* Midlatitude temperature variations in the Oligocene to Early Miocene. *Paleoceanogr. Paleoclimatol.* **34**, 1328–1343 (2019).

76. Śliwińska, K. K. *et al.* Sea surface temperature evolution of the North Atlantic Ocean across the Eocene-Oligocene Transition, *Clim. Past* **19**, 123–140 (2023).

77. Diester-Haass, L. & Zahn, R. Eocene-Oligocene transition in the Southern Ocean: history of water mass circulation and biological productivity. *Geology* **24**, 163–166 (1996).

630 78. Pusz, A. E., Thunell, R. C. & Miller, K. G. Deep water temperature, carbonate ion,
631 and ice volume changes across the Eocene-Oligocene transition. *Paleoceanography*
632 **26**, PA2205 (2011).

633 79. Scher, H. D. & Martin, E. E. Circulation in the Southern Ocean during the
634 Paleogene inferred from neodymium isotopes. *Earth Planet. Sci. Lett.* **228**, 391–
635 405 (2004).

636 80. Scher, H. D. & Martin, E. E. Oligocene deep water export from the North Atlantic
637 and the development of the Antarctic Circumpolar Current examined with
638 neodymium isotopes. *Paleoceanography* **23**, PA1205 (2008).

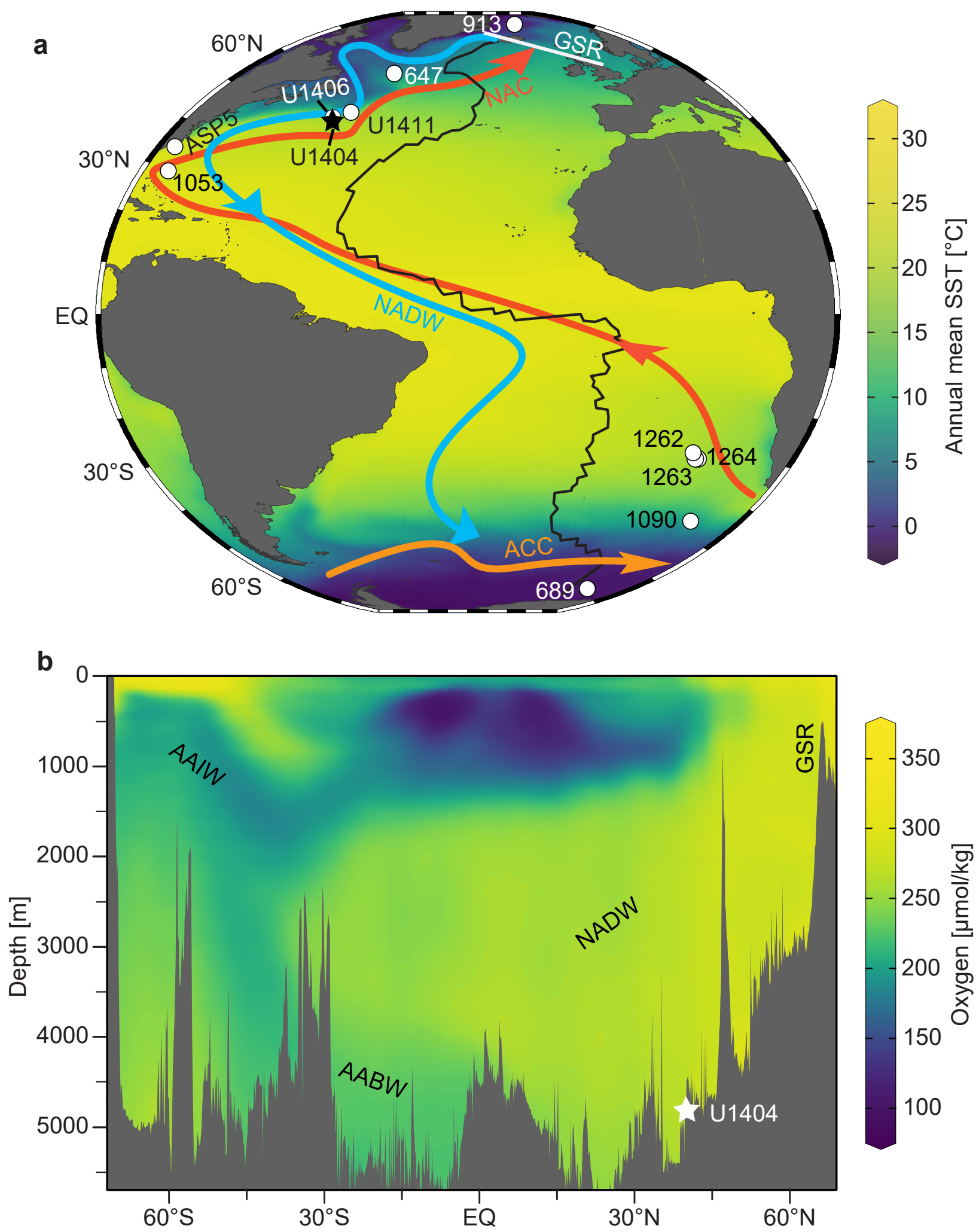
a
60°N
30°N
EQ
30°S
60°S
913
GSR
647
U1406
NAC
U1411
ASP5
U1404
1053
NADW
1262
1264
1263
1090
ACC
689
Annual mean SST [°C]
30
25
20
15
10
5
0
b
Depth [m]
0
1000
2000
3000
4000
5000
AAIW
GSR
NADW
AABW
U1404
60°S
30°S
EQ
30°N
60°N
Oxygen [µmol/kg]
350
300
250
200
150
100

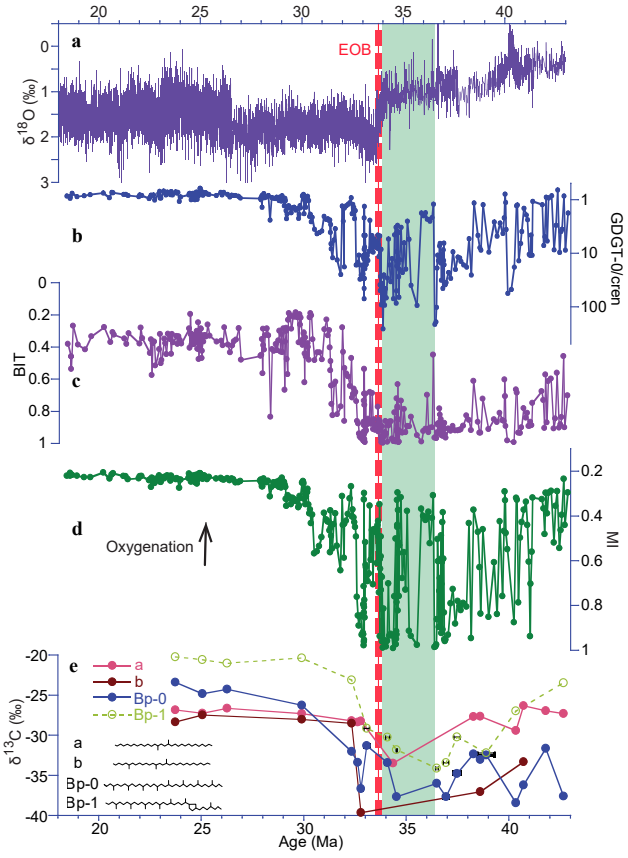
20
25
30
35
40
a
EOB
δ18O (‰)
0
1
2
3
b
GDGT-0/cren
1
10
100
BIT
c
0
0.2
0.4
0.6
0.8
1
d
Oxygenation
MI
0.2
0.4
0.6
0.8
1
e
a
b
Bp-0
Bp-1
δ13C (‰)
-20
-25
-30
-35
-40
Age (Ma)

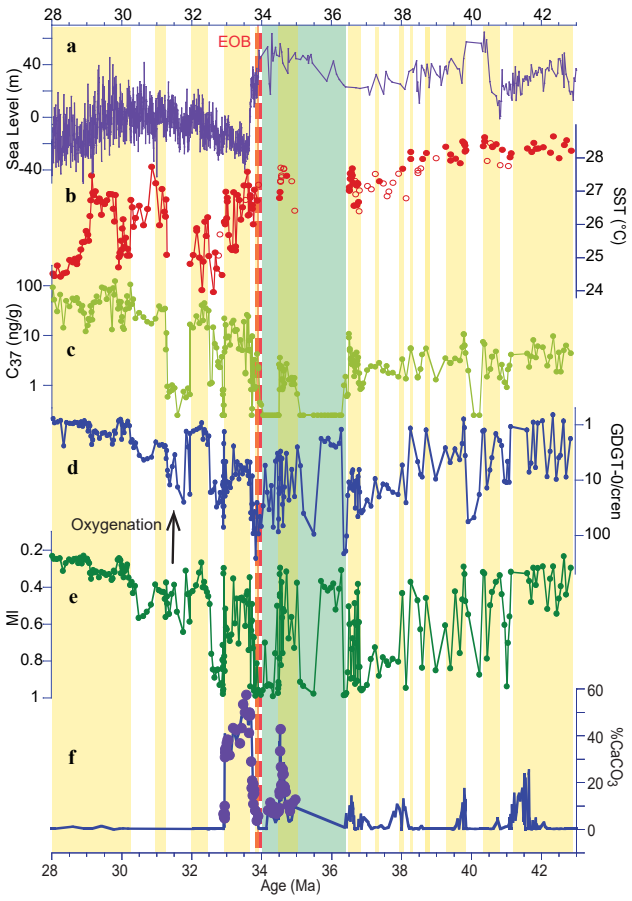
28
30
32
34
36
38
40
42
a
EOB
Sea Level (m)
40
0
-40
b
SST (°C)
28
27
26
25
24
c
C_{37} (ng/g)
100
10
1
d
GDGT-0/cren
1
10
100
Oxygenation
e
MI
0.2
0.4
0.6
0.8
1
f
%CaCO3
60
40
20
0
Age (Ma)

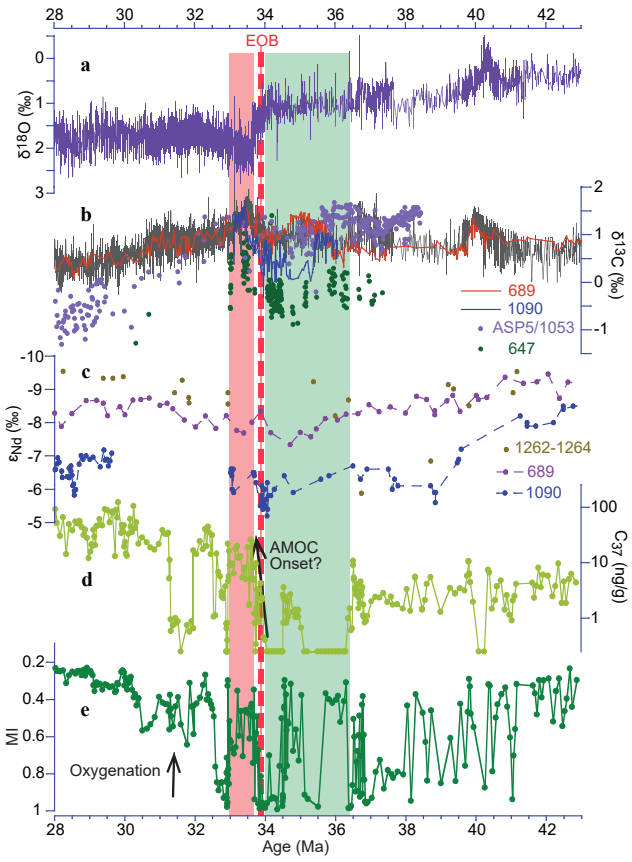
EOB
a
b
c
d
e
δ18O (‰)
δ13C (‰)
689
1090
ASP5/1053
647
εNd (‰)
1262-1264
689
1090
AMOC
Onset?
C37 (ng/g)
MI
Oxygenation
Age (Ma)

Isoprenoid

Archaeol
653.6

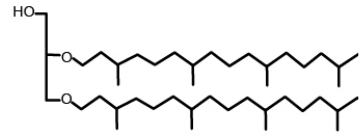

GDGT-0
1302.3

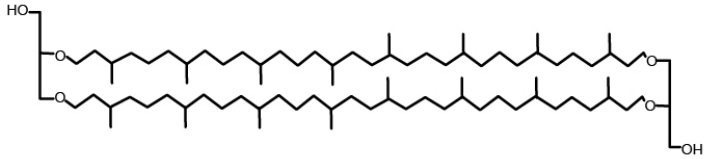

GDGT-1
1300.3

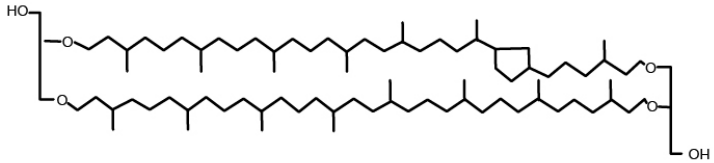

GDGT-2
1298.3

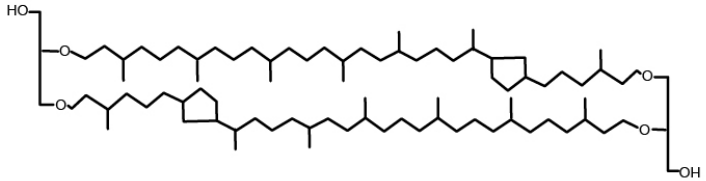

GDGT-3
1296.3

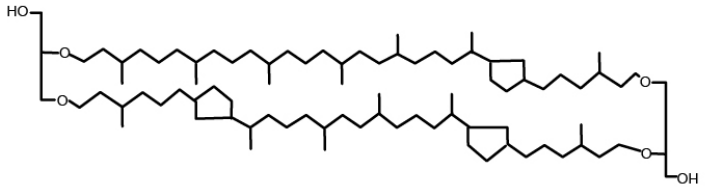

Crenarchaeol

Crenarchaeol'
1292.3

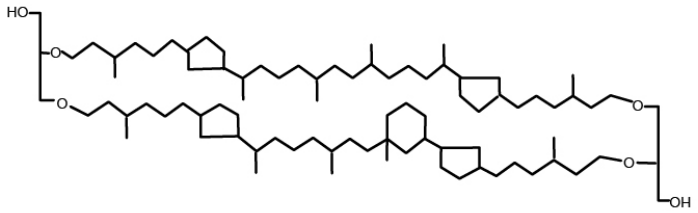

Branched

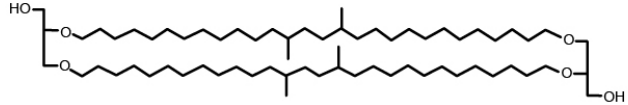

Ia
1022.0

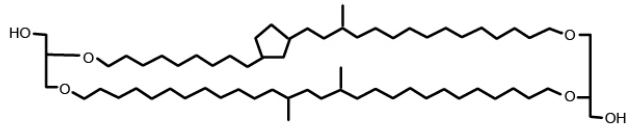

Ib
1020.0

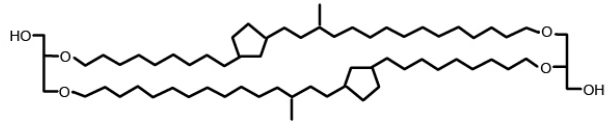

Ic
1018.0

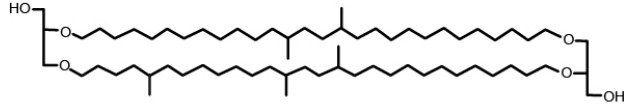

IIa
1036.0

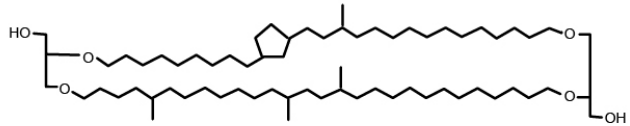

IIb
1034.0

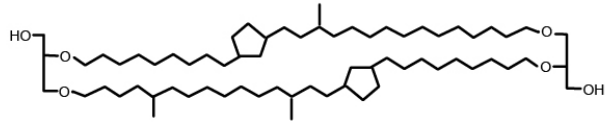

IIc
1032.0

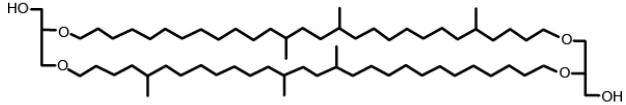

IIIa
1050.0

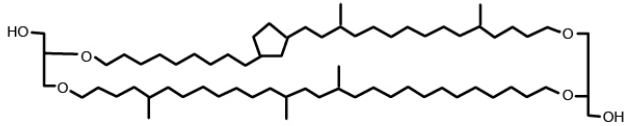

IIIb
1048.0

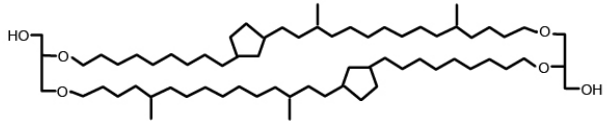

IIIc
1046.0

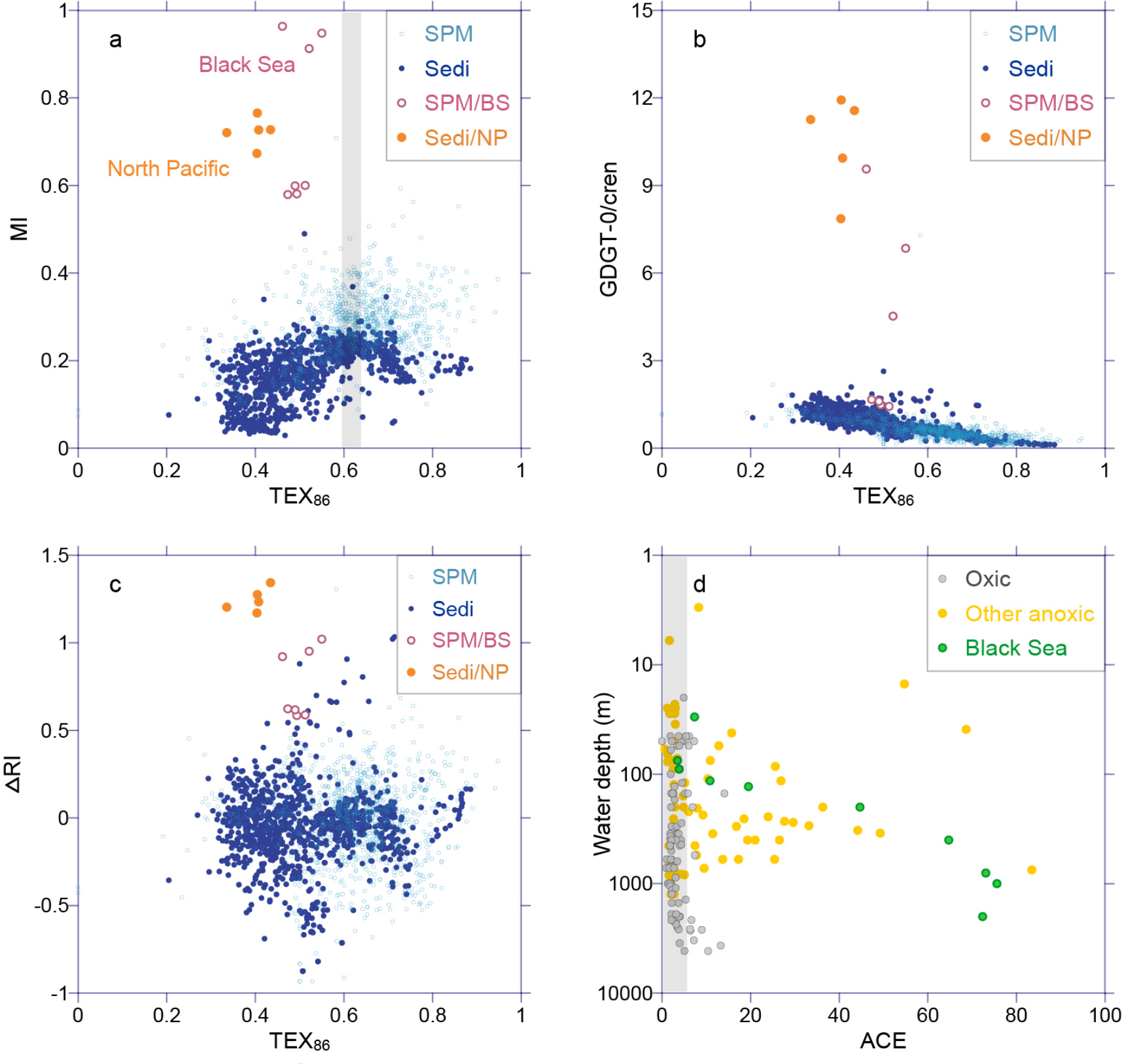
a
Black Sea
North Pacific
SPM
Sedi
SPM/BS
Sedi/NP
MI
TEX86
b
GDGT-0/cren
c
ΔRI
d
Oxic
Other anoxic
Black Sea
Water depth (m)
ACE

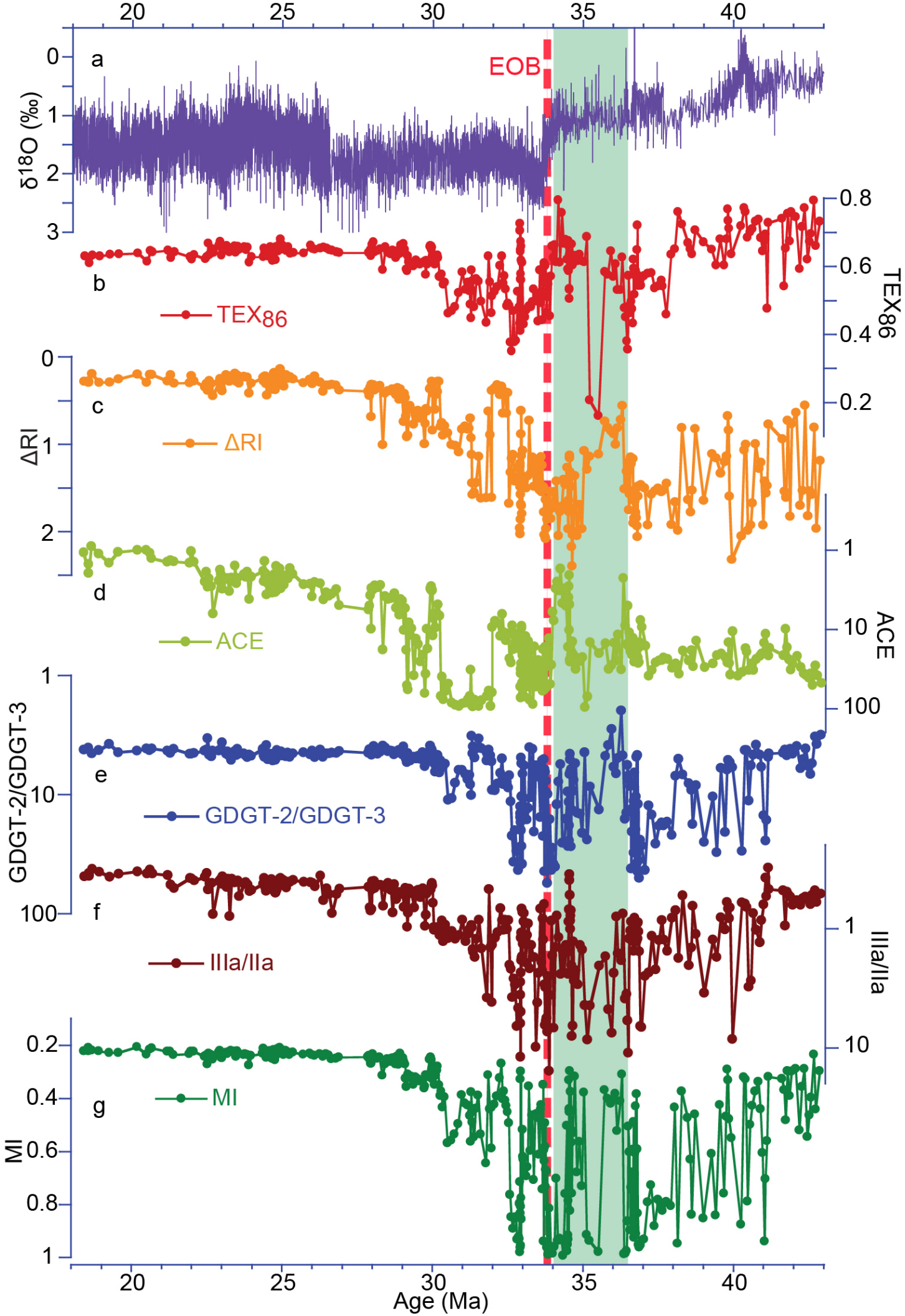
20
25
30
35
40
a
EOB
δ18O (‰)
0
1
2
3
b
TEX86
0.8
0.6
0.4
0.2
TEX86
c
ΔRI
0
1
2
ΔRI
d
ACE
1
10
100
ACE
e
GDGT-2/GDGT-3
1
10
100
GDGT-2/GDGT-3
f
IIIa/IIa
1
10
IIIa/IIa
g
MI
0.2
0.4
0.6
0.8
1
MI
20
25
30
35
40
Age (Ma)

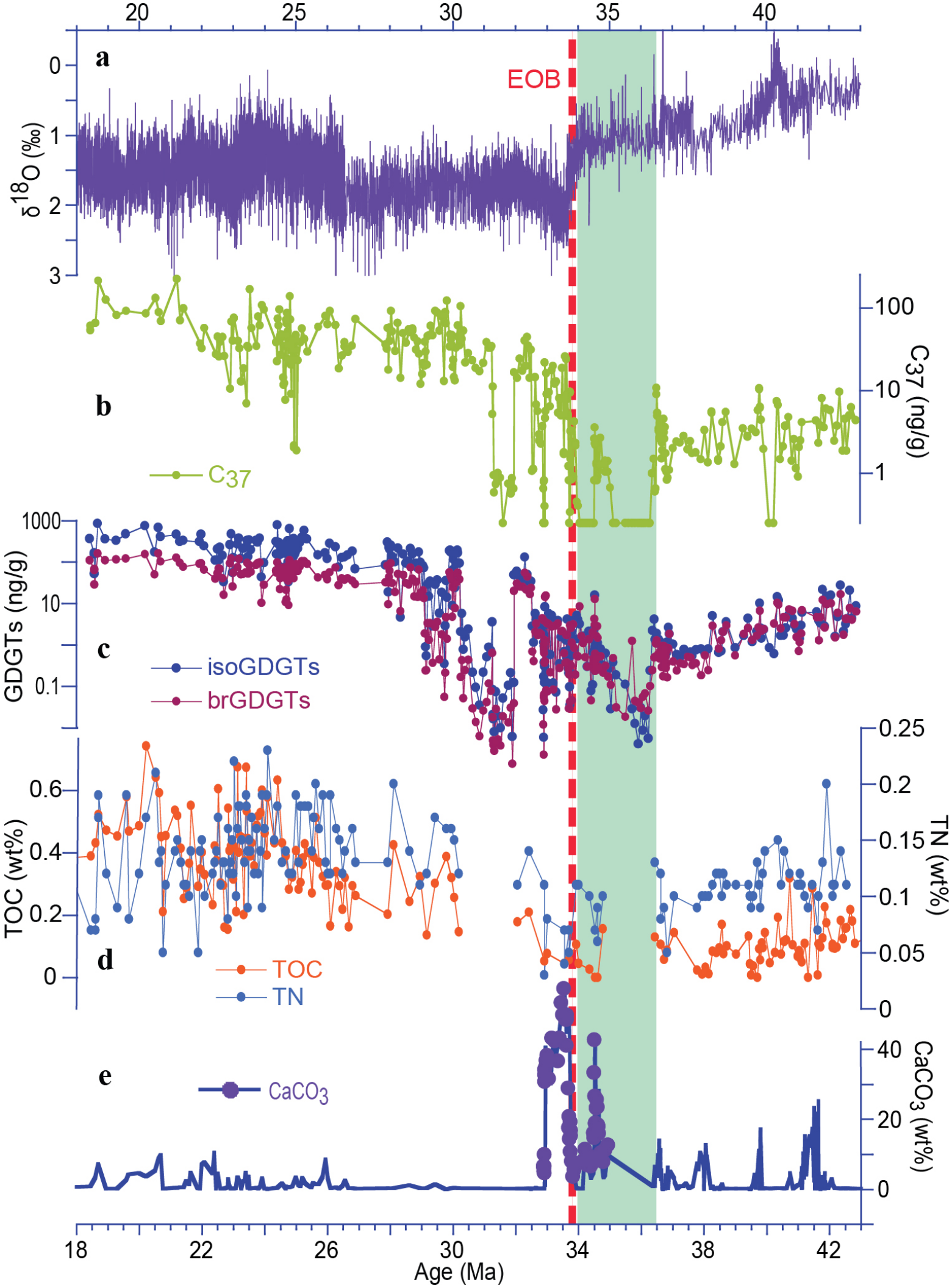
a
EOB
δ18O (‰)
b
C37
C37 (ng/g)
c
isoGDGTs
brGDGTs
GDGTs (ng/g)
d
TOC
TN
TOC (wt%)
TN (wt%)
e
CaCO3
CaCO3 (wt%)
Age (Ma)

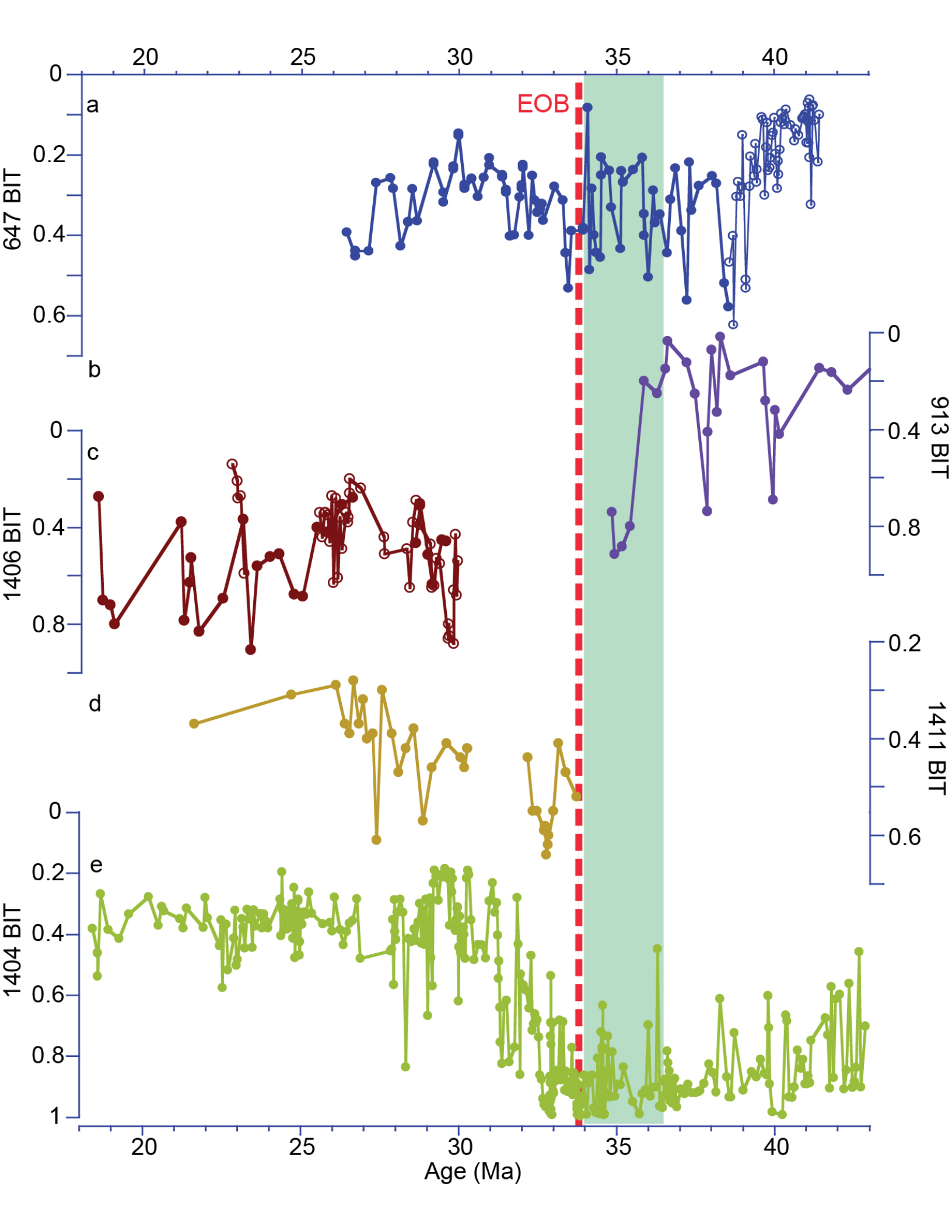
20
25
30
35
40
0
0.2
0.4
0.6
a
EOB
647 BIT
b
913 BIT
0.8
c
1406 BIT
d
1411 BIT
e
1404 BIT
1
Age (Ma)